

Turbulence and Sheared Flow in Fusion Plasmas

Carlos António Fragoso Ruivo
carlos.ruivo@ist.utl.pt

Instituto Superior Técnico, Lisboa, Portugal

October 2014

Abstract

The success of the fusion programme (namely ITER) depends on a better understanding of turbulent transport. In this context, it has been realised that radially sheared toroidal plasma flows can reduce radial turbulent transport. However, if the flow is too strongly sheared, it can introduce new instabilities. In addition, the presence of flow can lead to “subcritical turbulence”, i.e., turbulence that forms in the absence of any linearly unstable eigenmode. The aim of this project is to extend into the nonlinear regime previous studies performed with a minimal set of equations, which captures the interplay between two instabilities: the ITG instability, driven by the radial gradient in the ion temperature (“Ion-Temperature Gradient”), which is the principal cause of turbulent transport, and the PVG instability, driven by the radial gradient in the velocity parallel to the magnetic field (“Parallel Velocity Gradient”). For this purpose, a pre-existent numerical code was modified and extensively tested, to confirm previous studies made in the linear regime of these instabilities. Afterwards, the previous linear results were extended to the universal mode regime (driven solely by a density gradient), which is always stable in the set of equations considered. In the nonlinear regime, both the effect of the density drive on the nonlinear saturation plateau of the ITG and the inertial range on the nonlinear PVG energy spectrum was investigated. Even though these are low resolution, preliminary results (due to computation limitations), they anticipate interesting nonlinear behaviours of these instabilities, which will be examined in future work.

Keywords: fusion plasmas, turbulence, transport, sheared flow, ITG, PVG

1. Introduction

Plasma turbulence is driven by different free energy sources for micro-instabilities, mainly the inhomogeneity of plasma profiles including plasma temperature, density [1], and flow velocity. Understanding how this turbulence can be suppressed, since it leads to anomalously large radial transport coefficients, having thus deleterious effects on plasma confinement, is a central goal of fusion research. There are many examples regarding the effect of sheared flow on the neutralization of turbulence [2]. In [3], it was concluded that, for tokamaks, stabilization can occur through purely toroidal rotation. Indeed, shearing the turbulent eddies apart, in order for them to become smaller and smaller, can be made by a flow shear, therefore neutralizing turbulence [4]. Experimental results on DIII-D also confirm that toroidal shear flow can lead to stabilization [5], and anomalous transport is smaller than neoclassical transport [6]. In the LAPD (LArge Plasma Device), an experiment at UCLA, near-complete suppression of turbulence is observed for a given experimentally measured shear rate [7]. Moreover, tokamak discharges with improved energy confinement

properties arising from internal transport barriers (ITBs) have certain attractive features, such as a large bootstrap current fraction, which suggest a potential route to the steady-state mode of operation desirable for fusion power plants [8]. One major development on the investigation of transport barriers (regions of the plasma with very high temperature gradients), is the $\vec{E} \times \vec{B}$ shear stabilization model [6], in which the system self-organizes to reduce turbulence. However, shear flows parallel to the magnetic field can be destabilizing [9] and enhance turbulent transport, since they constitute a new source of free energy [3]. To sum up, on the one hand, perpendicular flow shear can be stabilizing, on the other hand, parallel flow shear can be destabilizing. Since the two are related, there is intense research to conclude what is the optimum shear flow for confinement.

A very interesting, and relatively unknown, topic of research is subcritical turbulence, that can arise even in the absence of any linearly unstable eigenmodes. Large flow shears come at a price of the PVG, driven by the velocity gradient, which is itself a source of free energy, that can give rise to

turbulence and anomalous transport. However, this instability is in fact also suppressed by flow shears, but only in the sense that no unstable modes survive at large enough velocity and small enough magnetic shear. Nevertheless, transient amplification is still possible. Therefore, these transiently growing modes can drive subcritical turbulence, whose amplitude increases with flow shear [10], limiting the effectiveness of differential rotation and the velocity shear to suppress anomalous transport [11, 12]. Previous studies referred in [13] discovered that the reason of these transient growth is the non-orthogonality of the eigenfunctions of the governing linear Vlasov operator, i.e. a non-normality of the linear operator.

2. Theoretical Framework

This work will focus on the effect of flow shear on the ion temperature instability in a fluid slab model, which is investigated in [14]. The system being studied consists of an infinite plasma slab subjected to an electrostatic perturbation in a sheared magnetic field (an extension to electromagnetic perturbations was recently made in [15]). In this model, the plasma is quasineutral consisting of two species: electrons and ions. The electrons have a Boltzmann response to the perturbing potential ϕ . The ions are described by collisional fluid equations, obtained from the gyrokinetic equation [16, 17, 18]. The detailed derivation of the equations of this model can be found in [14] and will not be repeated here. Only the basic assumptions and the key results will be presented.

2.1. Geometry

In this model, the sheared magnetic field is given by $\vec{B} = B_0[\hat{z} + (x/l_s)\hat{y}]$, where B_0 is a constant and l_s is the characteristic scale length of the magnetic field in the x -direction. Roughly speaking, x , y and z correspond to the radial, poloidal and toroidal directions in a tokamak, respectively. The sheared background flow field is given by $\vec{V}_0 = V_0(x/L_V)\hat{e}_V$, where L_V is the characteristic scale length of the flow variation in the x -direction and \hat{e}_V is a unit vector in the (y, z) -plane. The flow is thus a mixture of parallel (z -direction) and perpendicular (y -direction) flow. Following the reasoning of [19], the instabilities in the plasma due to the ITG are expected to have a short perpendicular wavelength (λ_x, λ_y) and a long parallel wavelength (λ_z), with respect to the magnetic field, so as to maximize motion in the vertical direction and minimize field line bending, and to be long and thin, $\lambda_y \ll \lambda_x \ll \lambda_z$. This is called a twisted-eddy representation. Nevertheless, short perpendicular wavelengths are rapidly sheared apart by the perpendicular component of the sheared flow. Hence, a coordinate transformation is required so that the flow is along the mag-

netic field lines and such that these field lines are coordinate lines, in order to remove the complications of both the magnetic field shear and the time dependence associated with the equilibrium flow. Therefore, the coordinate lines are aligned with the characteristics of the plasma response (only to electrostatic perturbations), particularly with the guiding center motion and propagation of sound waves [14]. Let us first consider the effect of magnetic field shear. The transformation used in [20] is

$$z^f = z, \quad y^f = y - \frac{x}{l_s}z, \quad x^f = x, \\ \vec{B} \cdot \nabla x^f = \vec{B} \cdot \nabla y^f = 0, \quad \vec{B} \cdot \nabla \equiv B_0 \frac{\partial}{\partial z^f}. \quad (1)$$

Secondly, the following time dependent transformation [14] is used, in order to include the effect of the sheared flow perpendicular to the magnetic field,

$$y^* = y - V_0 \frac{x}{L_V} (\hat{e}_V \cdot \hat{y})t. \quad (2)$$

The final coordinate transformation [20] is then a combination of both these transformations, yielding

$$t' = t, \quad z' = z + u_f t, \quad y' = y - \frac{x}{l_s}z', \quad x' = x, \quad (3)$$

where the velocity $u_f = V_0(l_s/L_V)\hat{e}_V \cdot \hat{y}$ is the velocity along the field line of twisting eddies, which represent the instabilities. Defining a Mach number M , one has that these eddies propagate at a speed $u_f = Mc_s$, according to equation (3), where c_s is the sound speed. The coordinate transformation and its effects are illustrated in Figure 1, taken from [14]. The axis origin is in the middle, the top corresponds to positive x and the bottom to negative x . When $t = 0$, $y^* = y$, according to equation (2), and as can be seen in Figure 1(a), one can sketch the flux tubes that represent the magnetic field. Cross-sections of the eddies are represented by red ovals for three positions in z . As has been referred, these eddies travel along these field lines. When $t = L_V/(V_0\hat{e}_V \cdot \hat{y})$, equation (2) yields $y^* = y - x$. At $x = 0$, $y^* = y$, flux tubes in the middle of Figure 1(b) remain unchanged. Let us consider that l_s and L_V are negative. Then, for positive x , $y^* = y - x$ means that the flux tube on top of Figure 1(b) goes to the right because of the sheared flow, as represented by the dot product $\vec{V}_0 \cdot \hat{y}$ (perpendicular component). For negative x , the flux tube goes to the left. The eddy is thus twisted because it is aligned with the field lines, and it propagates with velocity u_f . This “twisted-shearing” representation, in which the eddies are long and thin, twisting with the sheared magnetic field [19], used in [14], clarifies aspects of the physics

of sheared flows. Nevertheless, since it is a fluid model, it does not treat Landau damping nor does it capture ion finite Larmor radius (FLR), and so cannot model accurately fusion devices [14].

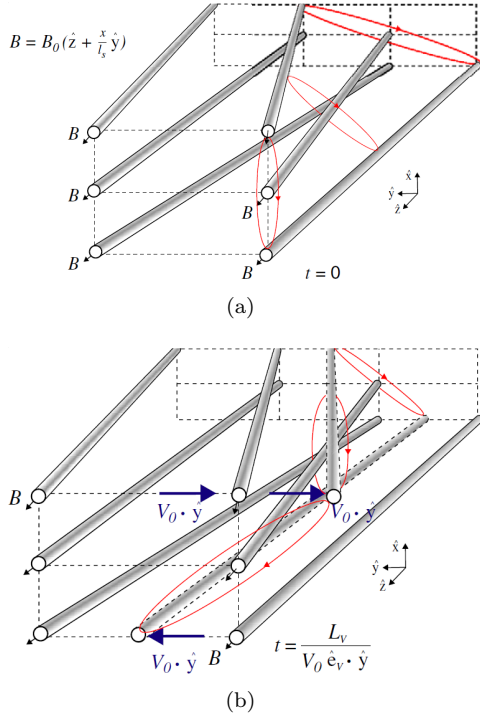


Figure 1: (a) Red ovals represent an eddy at $t = 0$. The sheared magnetic field is $\vec{B} = B_0[\hat{z} + (x/l_s)\hat{y}]$. (b) Twisting of the eddy, which propagates at a velocity u_f , parallel to \hat{x} due to the y (perpendicular) component of the sheared flow, at time $t = L_V/(V_0 \hat{e}_V \cdot \hat{y})$. Figure taken from [14].

2.2. System of equations

The drives of the ion response are, respectively, the background density and temperature gradients, plus the parallel flow shear,

$$\begin{aligned} \frac{1}{l_n} &= \frac{d}{dx} \ln n_0, & \frac{1}{l_T} &= \frac{d}{dx} \ln T_i, \\ \frac{1}{l_V} &= \frac{1}{L_V} \frac{V_0}{c_s} \hat{e}_V \cdot \hat{z}, & M &= \frac{u_f}{c_s}. \end{aligned} \quad (4)$$

In the collisional limit, the following order is considered, $\nu \gg \omega, \omega^*, v_{th} k_{\parallel}, u_f k_{\parallel}, \nu k^2 \rho^2$, where ν is the ion-ion collision frequency and ω^* represents the drift frequencies associated with the background gradients. Assuming that the equilibrium electron and ion temperatures are equal and denoted by T , $T_e = T_i = T$, imposing quasineutrality and introducing the normalizations

$$\begin{aligned} x' &= \rho_s \tilde{x}, & y' &= \rho_s \tilde{y}, & z' &= l_s \tilde{z}, & t &= \frac{l_s}{c_s} \tilde{t}, \\ \tilde{V} &= \frac{\delta V_{\parallel}}{c_s} \frac{l_s}{\rho_s}, & \tilde{T} &= \frac{\delta T}{T} \frac{l_s}{\rho_s}, & \tilde{n} &= \frac{\delta n}{n_0} \frac{l_s}{\rho_s}, \end{aligned} \quad (5) \quad \left(\frac{\partial}{\partial t} + M \frac{\partial}{\partial z} \right) V + \frac{3}{8} \frac{\partial}{\partial z} (2n + T) = i\omega_V^* n - \nu_{\perp} \tilde{\nabla}_{\perp}^2 V, \quad (12)$$

where $\rho_s = c_s/\Omega$ is the sound Larmor radius associated with the sound speed $c_s = \sqrt{(\gamma_e + \gamma_i)T/m}$, $\Omega = eB/m$ is the ion cyclotron frequency, m is the ion mass, the final set of equations are, dropping the tildes for convenience,

$$\left(\frac{\partial}{\partial t} + M \frac{\partial}{\partial z} \right) n + \frac{\partial V}{\partial z} = \frac{3}{8} \frac{l_s}{l_n} \frac{\partial n}{\partial y}, \quad (6)$$

$$\begin{aligned} \left(\frac{\partial}{\partial t} + M \frac{\partial}{\partial z} \right) V + \frac{3}{8} \frac{\partial}{\partial z} (2n + T) + \frac{3}{8} [n, V] = \\ \frac{3}{8} \frac{l_s}{l_V} \frac{\partial n}{\partial y} + \nu_{\perp} \nabla_{\perp}^2 V, \end{aligned} \quad (7)$$

$$\begin{aligned} \left(\frac{\partial}{\partial t} + M \frac{\partial}{\partial z} \right) T + \frac{2}{3} \frac{\partial V}{\partial z} + \frac{3}{8} [n, T] = \\ \frac{3}{8} \frac{l_s}{l_T} \frac{\partial n}{\partial y} + \chi_{\perp} \nabla_{\perp}^2 T, \end{aligned} \quad (8)$$

where n, V, T are, respectively, the perturbed density, velocity, and temperature, ν_{\perp} and χ_{\perp} are the diffusive viscosity and conductivity (that cause dissipation),

$$\nabla_{\perp}^2 = \frac{\partial^2}{\partial y^2} + \left(\frac{\partial}{\partial x} - z \frac{\partial}{\partial y} \right)^2, \quad (9)$$

and with the unit vector defined as $\vec{b} = \vec{B}/B$, for two arbitrary functions p and q the normalized Poisson bracket form is

$$[p, q] = (\nabla p \times \nabla q) \cdot \vec{b} = \frac{\partial p}{\partial x} \frac{\partial q}{\partial y} - \frac{\partial p}{\partial y} \frac{\partial q}{\partial x}. \quad (10)$$

Since the plasma is travelling along the field lines at a velocity u_f , one can define a normalized velocity M , with respect to the sound speed c_s , and so in equations (6)-(8), the time derivative has a convective form. As can be seen, the instability drives are represented by the first term on the right-hand side of each of equations (6)-(8), which express the convection of the equilibrium density, parallel velocity and temperature along their gradients by the perturbed $\vec{E} \times \vec{B}$ drift.

In order to linearise the system of equations (6)-(8), by taking the nonlinear terms $[n, V] = [n, T] = 0$, one makes all the fields to vary as $\exp[i(k_x x + k_y y)]$, multiplied by a function of z , to obtain

$$\left(\frac{\partial}{\partial t} + M \frac{\partial}{\partial z} \right) n + \frac{\partial V}{\partial z} = i\omega_n^* n, \quad (11)$$

$$\left(\frac{\partial}{\partial t} + M \frac{\partial}{\partial z}\right) T + \frac{2}{3} \frac{\partial V}{\partial z} = i\omega_T^* n - \chi_\perp \tilde{\nabla}_\perp^2 T, \quad (13)$$

with

$$\tilde{\nabla}_\perp^2 = k_x^2 + k_y^2(1 + z^2) - 2zk_x k_y, \quad (14)$$

$$\omega_n^* = \frac{3k_y l_s}{8 l_n}, \quad \omega_V^* = \frac{3k_y l_s}{8 l_V}, \quad \omega_T^* = \frac{3k_y l_s}{8 l_T}, \quad (15)$$

where ω_n^* , ω_V^* and ω_T^* are, respectively, the background driving gradients of density, parallel velocity and temperature. Considering the local, dissipationless form of equations (11)-(13), $\nu_\perp = \chi_\perp = 0$ and the terms explicitly proportional to z vanish. Solutions in the form $\exp[i(k_z z - \omega t)]$ can be considered. If one defines the frequency in the laboratory frame as $\omega' = \omega - k_z M$, the dispersion relation is

$$\omega'^2(\omega' + \omega_n^*) - \omega' k_z (k_z - \omega_V^*) + \frac{k_z^2}{4} \left(\frac{3}{2}\omega_T^* - \omega_n^*\right) = 0. \quad (16)$$

If the driving terms in density and parallel velocity are neglected, $\omega_n^* = \omega_V^* = 0$, the cubic dispersion relation for the collisional ion temperature gradient (ITG) is recovered [19],

$$\omega'^3 - k_z^2 \omega' + \frac{3}{8} k_z^2 \omega_T^* = 0. \quad (17)$$

If both the driving terms in density and temperature are neglected, $\omega_n^* = \omega_T^* = 0$, one has a quadratic dispersion relation,

$$\omega'^2 = k_z (k_z - \omega_V^*), \quad (18)$$

which describes the parallel velocity gradient (PVG) [3, 9]. Therefore, there is an instability if

$$\omega_V^* > k_z, \quad (19)$$

and thus the maximum growth rate is $\gamma_{max} = \omega_V^*/2$. Instability then results when the rate of increase in the flow by convection overcomes the deceleration due to the parallel pressure gradient, which occurs for $\omega_V^* > k_z$.

If only the drive in density is finite, $l_s/l_n \neq 0$, with $M = l_s/l_V = l_s/l_T = 0$, the dispersion relation is, divided by k_z^3 ,

$$\left(\frac{\omega}{k_z}\right)^3 + \frac{\omega_n^*}{k_z} \left(\frac{\omega}{k_z}\right)^2 - \frac{\omega}{k_z} - \frac{1}{4} \frac{\omega_n^*}{k_z} = 0, \quad (20)$$

and this cubic polynomial has no complex roots for any given value of ω_n^*/k_z , only real ones. This shows analytically that this case presents no instability, hence no universal instability [21] is possible.

However, since the governing operator of equations (11)-(13) is non-orthogonal in all cases, this allows for transient growth to occur, as has been referred in section 1.

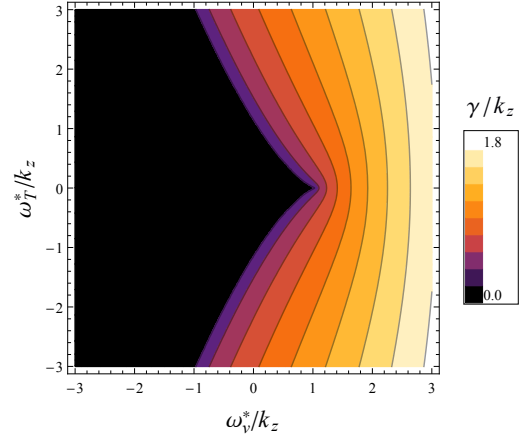


Figure 2: Maximum growth rate γ , obtained by solving equation (21) shows the interaction of the ITG (with drive ω_T^*) with the PVG (with drive ω_V^*) modes.

When $\omega_n^* = 0$, a contour plot of the maximum growth rate, $\gamma = \max[\text{Im}(\omega')]$, divided by k_z , is shown in Figure 2. Dividing equation (16) by k_z^3 , one obtains

$$\left(\frac{\omega'}{k_z}\right)^3 + \left(\frac{\omega_V^*}{k_z} - 1\right) \frac{\omega'}{k_z} + \frac{3}{8} \frac{\omega_T^*}{k_z} = 0, \quad (21)$$

so there is an instability, the PVG instability, if $\omega_V^* > k_z$, as seen from Figure 2, or

$$\left|\frac{\omega_T^*}{k_z}\right| > \frac{16}{9\sqrt{3}} \left(1 - \frac{\omega_V^*}{k_z}\right)^{3/2}, \quad (22)$$

upon solving for $\max[\text{Im}(\omega'_1), \text{Im}(\omega'_2), \text{Im}(\omega'_3)] > 0$, with respect to ω_T^*/k_z , where ω'_1, ω'_2 and ω'_3 are the three solutions to equation (21).

Defining the angles θ and θ_V , giving the direction of mode propagation and of the background flow, with respect to the magnetic field,

$$\tan \theta = \frac{k_y}{k_z}, \quad \frac{M}{(l_s/l_V)} \equiv \tan \theta_V = \frac{\hat{e}_V \cdot \hat{y}}{\hat{e}_V \cdot \hat{z}}, \quad (23)$$

where (4) was used, the instability criterion for the ω_V^* -driven instability (19) can be rewritten as

$$\omega_V^* = \frac{3}{8} k_y \frac{l_s}{l_V} = \frac{3}{8} k_z \tan \theta \frac{M}{\tan \theta_V} > k_z, \quad (24)$$

so

$$M > \frac{8 \tan \theta_V}{3 \tan \theta}. \quad (25)$$

2.3. Instability with $M = 0$

The following analytical case of instability with $M = 0$ was derived in [14]. We seek a solution that is required to be damped for large z , that is, $V \rightarrow 0$ as $|z| \rightarrow \infty$. By considering the case with no perpendicular flow shear, $M = 0$, the perturbation $k_x = 0$, maintaining only the viscous dissipation term, $\nu_\perp \neq 0$, $\chi_\perp = 0$ and by taking all fields to vary as $\exp(\gamma t)$, the perturbed parallel velocity can be written as

$$V = H_n \left[\left(\frac{a\nu_k}{b} \right)^{1/4} z \right] \exp \left(-\sqrt{\frac{a\nu_k}{b}} \frac{z^2}{2} + i \frac{\omega_V^* z}{2b} \right) \times \exp(\gamma t), \quad (26)$$

where H_n are the Hermite polynomials of order n , $\nu_k \equiv k_y^2 \nu_\perp$, and

$$a = \gamma - i\omega_n^*, \quad b = 1 + \frac{i}{4\gamma} \left(\frac{3}{2}\omega_T^* - \omega_n^* \right). \quad (27)$$

The growth rates satisfy

$$\frac{a}{b}(\gamma + \nu_k) + (2n + 1) \sqrt{\frac{a\nu_k}{b}} - \frac{\omega_V^{*2}}{4b^2} = 0. \quad (28)$$

2.4. Characteristics form

Defining

$$S = \frac{3}{2}T - n, \quad C^\pm = V \pm \frac{3}{4} \left(n + \frac{T}{2} \right), \quad (29)$$

equations (11)-(13) can be written in characteristics form as

$$\left[\frac{\partial}{\partial t} + M \frac{\partial}{\partial z} \right] S = i \frac{\omega_S^*}{2} \left(C^+ - C^- - \frac{S}{2} \right) - \frac{1}{2} \chi_\perp \tilde{\nabla}_\perp^2 \left(C^+ - C^- + \frac{3S}{2} \right), \quad (30)$$

$$\begin{aligned} \left[\frac{\partial}{\partial t} + (M \pm 1) \frac{\partial}{\partial z} \right] C^\pm = & i \frac{\omega_\pm^*}{2} \left(C^+ - C^- - \frac{S}{2} \right) - \frac{1}{2} \nu_\perp \tilde{\nabla}_\perp^2 (C^+ + C^-) \\ & \mp \frac{1}{8} \chi_\perp \tilde{\nabla}_\perp^2 \left(C^+ - C^- + \frac{3S}{2} \right), \end{aligned} \quad (31)$$

where

$$\omega_S^* = \frac{3}{2}\omega_T^* - \omega_n^*, \quad \omega_\pm^* = \omega_V^* \pm \frac{3}{4} \left(\frac{\omega_T^*}{2} + \omega_n^* \right). \quad (32)$$

When $M > 1$, the entropy wave S and the sound waves C^+ and C^- are propagating in the same direction, being dissipated further away along the field lines. When $M < 1$, S and C^+ are moving forward and C^- is moving backwards, therefore eigenmodes may be formed, by the combination of oppositely travelling waves. Even though for $M > 1$,

all characteristics propagate in the same direction, transient perturbations can still grow in the system for a finite time. Indeed, for $M \gg 1$, the initial perturbation is amplified by a factor of $\exp[\sqrt{M}]$ until $t = t_c = \sqrt{\gamma_0}/(\sqrt{\nu_k}M)$, where $\gamma_0 = \omega_V^*/2$ (growth rate for the PVG instability). Afterwards, the amplitude evolution decays as t^{-2} . However, as seen in equation (6), there is no explicit dissipation for the density perturbations, so they do not decay.

3. Code description

The numerical code used in this work is *Viriato* [22]. *Viriato* is a 3D code, pseudo-spectral in the xy plane and grid-based along the z direction. Domain decomposition with MPI is employed for parallelization. The code has been extensively benchmarked in several different plasma regimes, from reduced-MHD to low-beta reduced gyrokinetics [22, 23]. In this work, the code was modified to solve the set of equations (6)-(8). The equations are discretised on a grid, which has 3 dimensions: x , y and z , each of them with their own length L . Consider the grid in z , for instance. The equations have modes in z , $k_z = (2\pi/L_z)m_z$, where $1 \leq m_z \leq L_z/\Delta z = nlz$ is the number of modes, $\Delta z = L_z/nlz$ is the spatial resolution and nlz is the number of grid points. The characteristic equations, except for the dissipative terms, are integrated using a second-order upwind scheme [24], which naturally captures the forward or backward propagation of the characteristics. On the other hand, both the dissipative and nonlinear terms are solved using a predictor-corrector method, the Euler method with a trapezoidal rule, also known as Heun's method. In order to separate both these contributions to the equations, a Strang splitting scheme is used [23], dividing the calculation of the second-order upwind scheme into two steps of $\Delta t/2$. Since there are multiple processors, boundary conditions should consider the requirement of up to two known points in a neighbouring processor, given the second-order nature of this numerical scheme. For numerical stability, the CFL condition must be obeyed, so that the time step must satisfy

$$\Delta t = \alpha \min \left[\frac{1}{(\nu_\perp, \chi_\perp) \max[k_x^2 + k_y^2(1+z^2) - 2zk_xk_y]}, \frac{\Delta z}{M+1}, \frac{4}{\max(\omega_S^*)}, \frac{2}{\max(\omega_\pm^*)}, \frac{8}{3 \max(k_xk_y n)} \right], \quad (33)$$

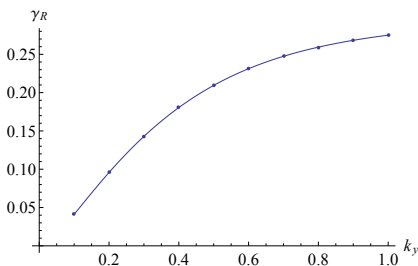
where $\alpha < 1$.

4. Linear results

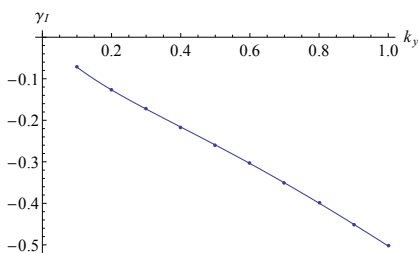
This section presents numerical experiments to solve equations (6)-(8), when $[n, V] = [n, T] = 0$.

In the case of instability with $M = 0$, the allowed growth rates are given in equation (28), and this analytical result will serve as a benchmark to the

developed code. For a given k_y , the growth rate γ can be obtained by solving equation (28) and comparing it with numerical data points whilst solving equations (11)-(13) with $M = \chi_\perp = k_x = 0$ numerically, for a given set of parameters, as is shown in Figure 3. When plotting the density n , for instance, as a function of time, for a given k_y , noticing that $\gamma = \gamma_R + i\gamma_I$, so $\exp(\gamma t) = \exp(\gamma_R t) \exp(i\gamma_I t)$, the fitting to be done to that curve is $\text{Re}[\exp(\gamma t)] = \exp(\gamma_R t) \cos(\gamma_I t)$, thus obtaining the parameters γ_R and γ_I . This procedure is repeated for different values of $k_y = 2\pi/L_y$. An example for $k_y = 0.3$ is shown in Figure 4. In this case, $L_z = 100$, $nlz = 1024$, $\Delta z = 0.1$, and the parameter used in the CFL condition (33) is $\alpha = 0.5$. The initial condition is $n(x, y, z, 0) = \cos(k_y y) \exp[-z^2/(2\sigma_z)]$, with $\sigma_z = 3$. The total CPU time used for each k_y was ~ 2 hours (16 processors used for 20 minutes). Figure 3 is a test to the code that has been developed. The numerical results show excellent agreement with the analytical result.



(a) Real part of γ as a function of k_y . Data points are the numerical result for each k_y and the line is the analytical curve.



(b) Imaginary part of γ as a function of k_y . Data points are the numerical result for each k_y and the line is the analytical curve.

Figure 3: Growth rate as a function of k_y . The parameters used to obtain γ , analytically with $n = 0$ (shown with a solid line) from equation (28), and numerically (shown with dots) from equations (11)-(13) are: $M = \chi_\perp = k_x = 0$, $l_s/l_n = 3$, $l_s/l_T = 6$, $l_s/l_V = 9$, $\nu_\perp = 3$, $\chi_\perp = 0$.

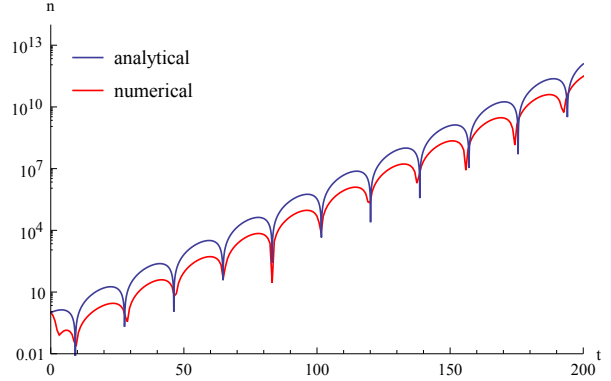


Figure 4: Time trace of the density for the mode $k_y = 0.3$. The analytical expression $\text{Re}(\gamma(k_y = 0.3)) = e^{0.14t} \cos(0.17t)$ (blue), obtained from equation (28), is plotted against the numerical result (red), obtained by solving equations (11)-(13) with the parameters shown in Figure 3. Note that there is an initial transient in the numerical plot.

4.1. Linear results with only finite l_s/l_n

The time trace of the density in the case of only finite $l_s/l_n = 100$, with all other drives set to zero and $M = 0$, is shown in Figure 5. No instability is observed. Indeed, the frequencies for the waves obtained satisfy the dispersion relation (20). In this case, $L_z = 100$, $nlz = 256$, $\Delta z = 0.39$, $L_y = 40\pi$, $nly = 32$, $\Delta y = 3.93$, $L_x = 2\pi$, $nlx = 8$, $\Delta x = 0.79$ and $\alpha = 5 \times 10^{-4}$. The initial condition is $n(x, y, z, 0) = \exp[-y^2/(2\sigma_y)] \exp[-z^2/(2\sigma_z)]$, with $\sigma_y = \sigma_z = 3$. The modes captured in y are thus $k_y = (2\pi/40\pi)m_y = 0.05m_y$, with $1 \leq m_y \leq 32$. The total CPU time used was ~ 768 hours for reaching $t \sim 200$ (32 processors used for 24 hours). Since no initial condition was given for x , there is no temporal nor spatial evolution in this direction. As $M = 0$, there is no propagation of the Gaussian in the z direction. The initial condition drifts in the y -direction and, since the boundary conditions are periodic, the perturbation is observed repeatedly, as shown by the peaks in Figure 5.

4.2. Linear instabilities and transient region

Consider now the linear set of equations (11)-(13). Figure 6, taken from [14], illustrates the maximum growth rate as a function of M and l_s/l_T for fixed $l_s/l_V = 30M$ and $l_s/l_n = 0$, showing the competition between the ITG and PVG instabilities. In fact there are three regions to be considered: two of linear instability, ITG (on the top) and PVG (on the bottom); and transient, where there are no linear instabilities present (on the middle). Henceforth, all simulations were made at fixed $\nu_\perp = 3$ and $\chi_\perp = 10/3$.

Evaluating first the ITG region, with $M = 0.3$, $l_s/l_V = 30M$ and $l_s/l_T = 45$ (see Figure 6), the

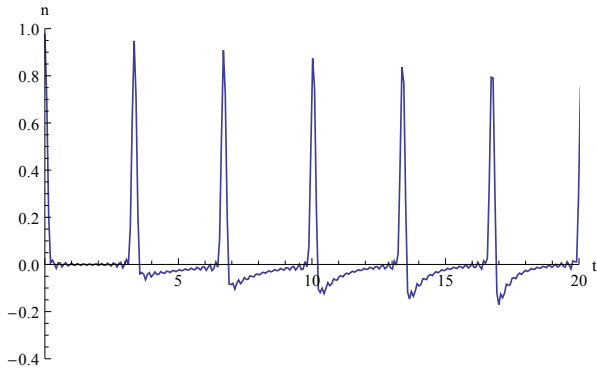


Figure 5: Time trace of the density, upon solving equations (11)-(13) with $M = l_s/l_V = l_s/l_T = \nu_\perp = \chi_\perp = 0$ and $l_s/l_n = 100$.

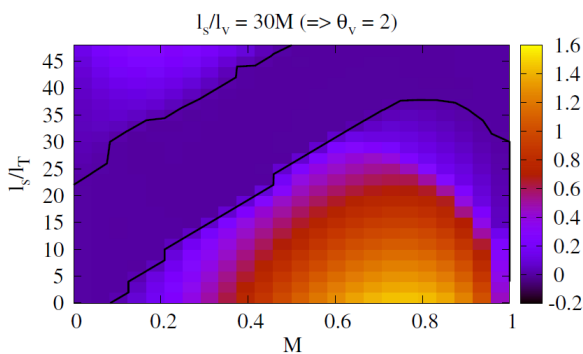


Figure 6: Maximum growth rate as a function of M and l_s/l_T , with $l_s/l_V = 30M$, for a conventional large aspect ratio tokamak ($\theta_V = \arctan(1/30) \approx 2$, according to (23), so the flow is nearly parallel to the magnetic field). The parameters used were $L_z = 400$ and $\Delta z = 0.1$. Figure taken from [14].

maximum growth rate is indeed $\gamma_{max} = 0.17$, as stated by [14], for the mode $k_y = 0.3$, which is captured by the Gaussian in y used as an initial condition, and is shown in Figure 7. In this case, $L_z = 100$, $nlz = 1024$, $\Delta z = 0.1$, $L_y = 2\pi(10/3)$, $nly = 4$, the modes captured by the Gaussian in y are $k_y = 0.3m_y$, $\Delta y = 5.24$ and $\alpha = 0.5$. Since few grid points were used in y , this result is preliminary, with low resolution, and a confirmation of this result should be made. Nevertheless, the maximum growth rate obtained in this case was the same as in [14]. In this case, the total CPU time used was ~ 128 hours (64 processors used for 2 hours).

The other region with linear instability is the PVG region, with a growth rate shown in Figure 8. The maximum growth rate is not in accordance with Figure 6, which shows a maximum growth rate of ~ 0.5 . Even though the resolution in z is the same as in [14], the box used is smaller, so the same modes in z are not being captured (compare $L_z = 400$ in [14] with $L_z = 100$ in this the-

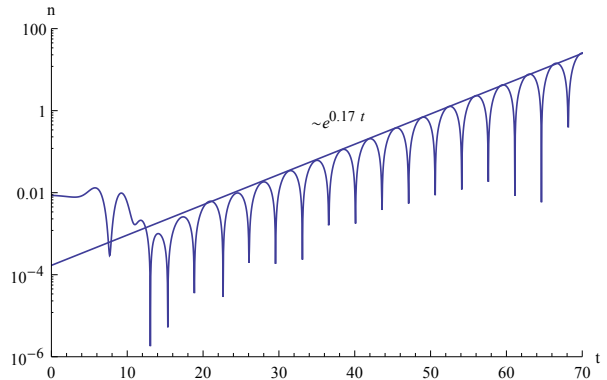


Figure 7: Time trace of the density for the ITG. The maximum growth rate is $\gamma_{max} = 0.17$. The parameters used were $M = 0.3$, $l_s/l_n = 0$, $l_s/l_V = 30M$, $l_s/l_T = 45$ (see Figure 6).

sis), in order to work with $nlz = 1024$ instead of $nlz = 4096$. If these were the case, the simulation would take $\sim 4^2 = 16$ more CPU hours to run. Indeed, in the CFL condition specified in (33), the term $\max \nabla_\perp^2$ has a $\max(z^2) = L_z^2/4$ contribution to it, as seen from (14), so the time step is influenced by this term and decreases as $\sim L_z^{-2}$. However, if the diffusive terms of equations (12)-(13) are treated with an implicit Crank-Nicolson scheme [23], the explicit $\sim L_z^{-2}$ dependence of the time step can be avoided, thus improving the computing time. Furthermore, the modes in y used here are $k_y = (2\pi/40\pi)m_y = 0.05m_y$, so the only values of k_y that are captured are from 0.05 to 1.6, in steps of 0.05, since $nly = 32$. To sum up, the grid specifications for y and z used in this thesis are not the same as those used in [14]. Therefore, the maximum growth rate is not the same. In this case, the total CPU time used was ~ 6144 hours (256 processors used for 24 hours).

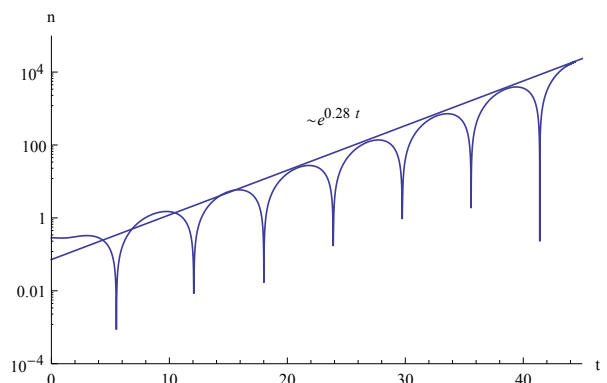


Figure 8: Time trace of the density for the PVG. The parameters used were $M = 0.3$, $l_s/l_n = 0$, $l_s/l_V = 30M$ (see Figure 6).

The temporal evolution of the density and veloc-

ity in the transient region is shown in Figure 9. As can be seen from Figure 6, there are no linearly unstable eigenmodes in the transient region, so Figure 9 shows transient amplification. In order to observe a decay of the velocity due to dissipative terms, as shown in equation (7), as opposed to the density, which has no explicit dissipation, as seen from (6), the simulation should have been run longer. The grid specifications used were the same as for the PVG case, except that $L_y = 10\pi$ and $nly = 8$. In this case, the total CPU time used was ~ 1536 hours (64 processors used for 24 hours).

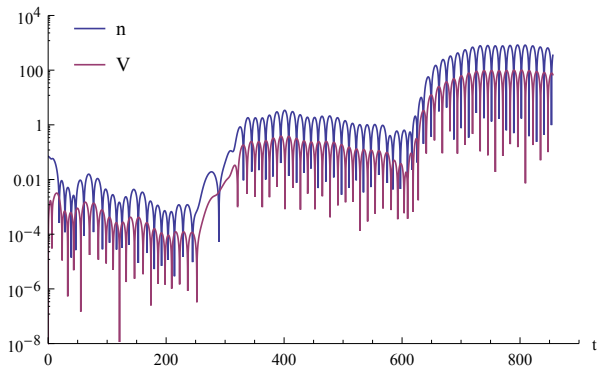


Figure 9: Time trace of the density (blue) and velocity (red) for the transient region. The parameters used were $M = 0.3$, $l_s/l_n = 0$, $l_s/l_V = 30M$, $l_s/l_T = 20$ (see Figure 6).

5. Nonlinear results

This section presents numerical experiments to solve equations (6)-(8), when $[n, V] \neq 0$ and $[n, T] \neq 0$.

5.1. Nonlinear ITG with finite l_s/l_n

The nonlinear results for the case of the ITG for 11 values of the density drive, from $l_s/l_n = 0$ to $l_s/l_n = 10$, are presented here. A comparison is made between $l_s/l_n = 0$ and $l_s/l_n = 3$ in Figure 10. The initial condition is $n(x, y, z, 0) = 10^{-2} \cos(k_x x) \exp[-y^2/(2\sigma_y)] \exp[-z^2/(2\sigma_z)]$, with $k_x = 1$ and $\sigma_y = \sigma_z = 3$. The parameters used were $L_x = 2\pi$, $nlx = 8$, $\Delta x = 0.79$, and the other grid specifications were the same as for the linear ITG case. These are preliminary, low resolution results. In this case, the total CPU time used was ~ 1024 hours (64 processors used for 16 hours).

The linear growth rate increases with the density drive, as shown in Figure 11. The vertical dashed lines in Figure 10 show that, for $l_s/l_n = 0$, the nonlinear saturation plateau starts at $t = 75$ and for $l_s/l_n = 3$ at $t = 62$. In the nonlinear regime, the value of the time-averaged density in the saturated turbulent regime, n_{sat} , is calculated via the weighted arithmetic mean $n_{sat} =$

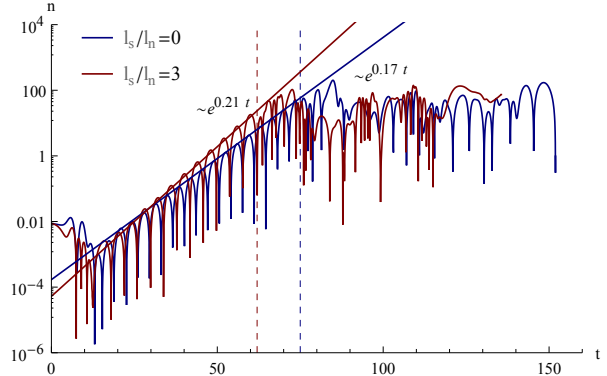


Figure 10: Time trace of the density, with $M = 0.3$, $l_s/l_V = 30M$ and $l_s/l_T = 45$ (ITG region, see Figure 6), comparing the cases $l_s/l_n = 0$ (blue) with $l_s/l_n = 3$ (red). The linear growth rates for both these cases are shown. Afterwards, the nonlinear regime is characterised by a saturation plateau, which starts at $t = 75$ for $l_s/l_n = 0$ and at $t = 62$ for $l_s/l_n = 3$, as marked by the vertical dashed lines.

$(\sum_{i=1}^k n_i t_i) / (\sum_{i=1}^k t_i)$, where k is the total number of points used in the plot, starting from the beginning of the saturation plateau (see Figure 12). The commonly accepted saturation mechanism of the nonlinear ITG are zonal flows [25], which needs to be confirmed in the considered system.

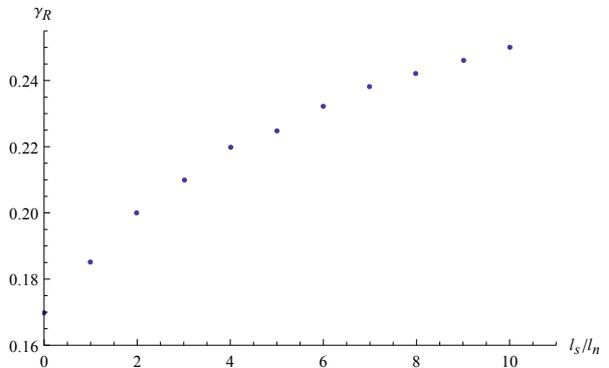


Figure 11: Linear growth rate as a function of the density drive.

5.2. Nonlinear PVG

In the case of the nonlinear PVG, the time trace of the density is shown in Figure 13. The initial condition is the same as in the nonlinear ITG case, except that a Gaussian was used for x , and the grid specifications are $L_x = L_y = L_z = 2\pi$, $nlx = nly = nlz = 64$, $\Delta x = \Delta y = \Delta z = 0.1$ and $\alpha = 0.1$. The parameter L was reduced in all directions, in order to have higher resolution results, and all Gaussian standard deviations were changed to $\sigma = 0.1$. In this case, the total CPU time used was ~ 9216 hours

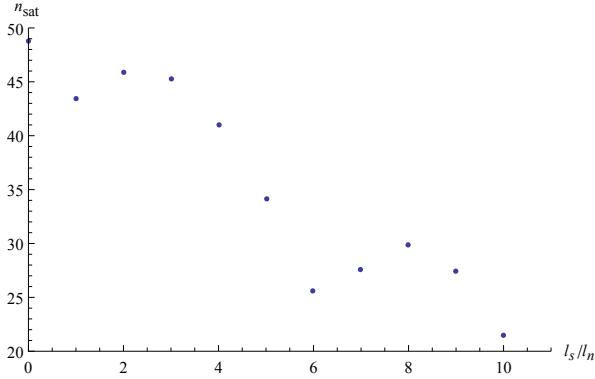


Figure 12: Time-averaged density in the saturated turbulent regime (note the saturation plateau as in Figure 10, for instance) as a function of the density drive.

(512 processors used for 18 hours).

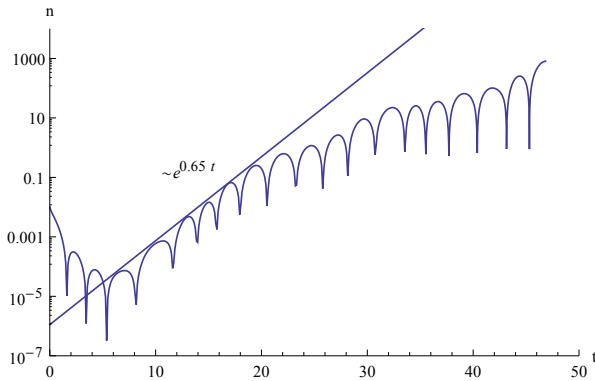


Figure 13: Time trace of the density, with $M = 0.3$, $l_s/l_V = 30M$ and $l_s/l_T = 5$ (PVG region, see Figure 6). The linear growth rate is shown.

The energy spectrum E vs k_\perp is shown in Figure 14, where $E = |k_\perp n|^2$ and $k_\perp = \sqrt{k_x^2 + k_y^2}$. For $t = 30.084$, the energy spectrum is shown to decay as k_\perp increases, as expected. There is an increasing energy peak at times $t = 42.106$ and $t = 46.797$, which is the manifestation of lack of convergence of the numerical method. One possible explanation for this fact can be the following. Dissipation occurs far along the field lines, as has been mentioned, as does the shearing of the eddy. Indeed, for large z , the dissipative terms in equations (12)-(13) are the dominant ones. Since $L_z = 2\pi$ is small for the system being considered, there is an increasing accumulation of energy with time, which is not being dissipated, as the observed energy peak shows. As for the inertial range observed in Figure 14, limited by vertical dashed lines, for both $t = 42.106$ and $t = 46.797$, there is not, as yet, any explanation for the value of the observed power law slope. However,

in this case, the slope keeps changing in time due to the energy accumulation (bottleneck) at small scales (a non-physical effect), so it is not possible to clearly identify the correct power law index.

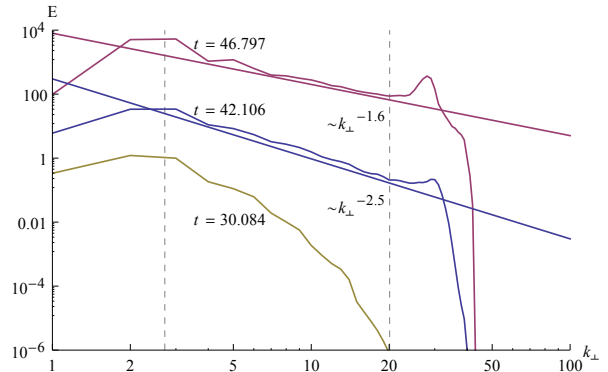


Figure 14: Energy spectrum E vs k_\perp for the nonlinear PVG at times $t = 30.084$ (yellow), $t = 42.106$ (blue) and $t = 46.797$ (red). Both the blue and red curves have an inertial region, limited by vertical dashed lines, that fit a power law of $k_\perp^{-2.5}$ and $k_\perp^{-1.6}$, respectively. The energy spectrum for $t = 30.084$ is shown to decay as k_\perp increases, as expected.

6. Conclusions

In this work, theoretical and numerical (high-performance computing) studies were performed on the effect of background sheared flows on the linear and nonlinear evolution of microinstabilities in magnetic confinement fusion plasmas. The first stage of the project consisted of modifying an existing code to simulate the equations of reference [14] and being introduced to parallel programming and basic usage of supercomputing systems. The second stage was the benchmarking of the code against known analytical results. The third stage was to perform nonlinear simulations and analyse the results. The case for the instability with $M = 0$, presented here and derived analytically in [14], was numerically confirmed in section 4, thus obtaining a benchmark of the developed code. With only finite density drive, i.e., without the drives in velocity nor temperature, there is not any observed instability. This was shown for $l_s/l_n = 100$ in Figure 5. The maximum growth rate for the ITG of $\gamma_{max} = 0.17$ was obtained, as seen in Figure 6, in accordance with [14]. Nevertheless, for the PVG linear instability, as the dimensions of the grid were different in y and z , the maximum growth rate obtained in this thesis was different from the one obtained in [14]. In the transient region, where there are no unstable eigenmodes present, transient amplification was obtained, as seen in Figure 9. As far as the nonlinear results are concerned, it was observed a saturation plateau for the nonlinear ITG case and the varia-

tion of the density drive influenced both the linear growth rate and the value of the density saturation in the nonlinear regime (see Figures 10–12). The energy spectrum E vs k_{\perp} for the nonlinear PVG (see Figure 14) showed an inertial range, limited by vertical dashed lines, followed by an increasing energy peak, caused by an accumulation of energy, which is not being dissipated, as discussed. Higher resolution results are needed to confirm these nonlinear results. Using the fluid model presented in this thesis, future work involves performing linear simulations that capture the most unstable modes for the PVG region of Figure 6, and running simulations in the transient region for longer time than that shown in Figure 9, so that it is seen that the density does not decay and the velocity does. In the nonlinear regime, it remains to be seen how the PVG instability saturates and the ITG results need to be confirmed at higher resolutions. The influence of the density drive for both linear and nonlinear results can be studied as well. This was only done for the linear and nonlinear ITG regimes. Moreover, the nonlinear saturation of the ITG by zonal flows needs to be confirmed in the considered system. Furthermore, nonlinear simulations performed in the transient regime should show the manifestation of subcritical turbulence. The transitory solution referred here in section 2.4 and derived in [14] can be also confirmed numerically. A solution to avoid the explicit L_z^{-2} dependence of the time step, thus improving the computing time can also be implemented as a future work. This thesis focused on a simple fluid model. Once the nonlinear regime is understood, one could use these results as guidance to explore similar results with a fully gyrokinetic code, in proper tokamak geometry.

Acknowledgements

I would like to thank my supervisor, Professor Nuno Loureiro, and all my friends and family for their support. The computing time used in this thesis was provided by the Helios supercomputer at IFERC-CSC under projects GKMSC and VIRIATO.

References

- [1] E. J. Doyle *et al* (2007), *Nucl. Fusion*, **47**, S18S127
- [2] P. W. Terry (2000), *Rev. Mod. Phys.*, **72**, 109
- [3] F. L. Waelbroeck *et al* (1992), *Phys. Fluids*, B **4**, 2441
- [4] H. Biglari, P. H. Diamond (1990), *Phys. Fluids*, B **2**, 1
- [5] P. A. Politzer *et al* (2008), *Nucl. Fusion*, **48**, 075001
- [6] K. H. Burrell (1997), *Phys. Plasmas*, **4**, 1499
- [7] D. A. Schaffner *et al* (2012), *Phys. Rev. Lett.*, **109**, 135002
- [8] J. W. Connor *et al* (2004), *Nucl. Fusion*, **44**, R1-R49
- [9] P. J. Catto, M. N. Rosenbluth and C. S. Liu (1973), *Phys. Fluids*, **16**, 171929
- [10] M. Barnes *et al* (2011), *Phys. Rev. Lett.*, **106**, 175004
- [11] A. A. Schekochihin, E. G. Highcock and S. C. Cowley (2012), *Plasma Phys. Control. Fusion*, **54**, 055011
- [12] E. G. Highcock *et al* (2012), *Phys. Rev. Lett.*, **109**, 265001
- [13] V. Ratushnaya and R. Samtaney (2014), *ArXiv e-prints*, **1408.6631**
- [14] S. L. Newton, S. C. Cowley and N. F. Loureiro (2010), *Plasma Phys. Control. Fusion*, **52**, 125001
- [15] M. D. J. Cole *et al* (2014), *Plasma Phys. Control. Fusion*, **56**, 015007
- [16] E. A. Frieman and Liu Chen (1982), *Phys. Fluids*, **25**, 502
- [17] I. G. Abel *et al* (2013), *Rep. Prog. Phys.*, **76**, 116201
- [18] I. G. Abel and S. C. Cowley (2013), *New J. Phys.*, **15**, 023041
- [19] S. C. Cowley, R. M. Kulsrud and R. Sudan (1991), *Phys. Fluids*, B **3**, 2767
- [20] G. G. Howes and S. C. Cowley (2001), *Astrophys. J.*, **560**, 617-629
- [21] K. T. Tsang *et al* (1978), *Phys. Rev. Lett.*, **40**, 327
- [22] <http://web.ist.utl.pt/nuno.f.loureiro/Site/VIRIATO.html>
- [23] N. F. Loureiro and G. W. Hammett (2008), *Journal of Computational Physics*, **227**, 4518-4542
- [24] C. Hirsch, *Numerical Computation of Internal and External Flows, Volume 1: Fundamentals of Numerical Discretization*, John Wiley & Sons, 1988
- [25] P. H. Diamond *et al* (2005), *Plasma Phys. Control. Fusion*, **47**, R35-R161